

Cyclic liquefaction of a granular assembly under initial static shear stress: a DEM study

Ali Salehi Sichani

University of British Columbia, Vancouver, BC, Canada

Ming Yang

Northwestern University, Evanston, IL, USA

Mahdi Taiebat

University of British Columbia, Vancouver, BC, Canada



GeoCalgary
2022 October
2-5
Reflection on Resources

ABSTRACT

We adopt a three-dimensional discrete element method to investigate the behavior of dense granular materials subjected to constant volume cyclic triaxial shearing. The effect of initial static shear stress on the cyclic response is studied for relatively dense states by cyclic shearing of anisotropically compressed samples. The simulations show two deformation modes of cyclic mobility and residual deformation accumulation depending on the magnitudes of initial static shear stress and the amplitude of cyclic shear stress. By analyzing the axial strain development, we observe that the double amplitude axial strain increases with the number of loading cycles, presumably toward a saturation level in the residual deformation accumulation mode. From the micromechanics perspective, we observe that cyclic mobility mode is associated with a transient collapse of the contact network. In contrast, the contact network remains stable during the shearing process in the residual deformation accumulation mode.

RÉSUMÉ

Nous adoptons une méthode d'éléments discrets en trois dimensions pour étudier le comportement de matériaux granulaires denses soumis à un cisaillement triaxial cyclique à volume constant. L'effet de la contrainte de cisaillement statique initiale sur la réponse cyclique est étudié pour des états relativement denses par cisaillement cyclique d'échantillons comprimés de manière anisotrope. Les simulations montrent deux modes de déformation de mobilité cyclique et d'accumulation de déformation résiduelle en fonction de l'amplitude de la contrainte de cisaillement statique initiale et de l'amplitude de la contrainte de cisaillement cyclique. En analysant le développement de la déformation axiale, nous observons que la déformation de cisaillement à double amplitude augmente avec le nombre de cycles de chargement, vraisemblablement vers un niveau de saturation dans le mode de déformation résiduelle. Du point de vue de la micromécanique, nous observons que le mode de mobilité cyclique est associé à un effondrement transitoire du réseau de contact. En revanche, le réseau de contact reste stable pendant le processus de cisaillement en mode d'accumulation de déformation résiduelle.

1 INTRODUCTION

Strong dynamic shaking can induce liquefaction in soil deposits, that often manifests as excess pore pressure development, shear strength reduction, and large shear strain accumulation. Many researchers have used various physical tests through laboratory element level experiments and more recently various virtual numerical tests through discrete element simulations to investigate the mechanisms involved in the liquefaction triggering and post-liquefaction deformations. In undrained cyclic shearing and under level ground conditions, the contractive response of sands can bring the effective stress nearly to zero, hence liquefying the material. In this condition depending on the density, the material may experience flow liquefaction or cyclic mobility. Under sloping ground condition, depending on the magnitude of the initial static shear stress representing the slope, and the amplitude of the cyclic shear stress, one may observe the two deformation modes mentioned above, or a residual deformation accumulation without even reaching liquefaction in the sense of effective stress reduction to nearly zero (e.g., Vaid and Chern, 1983; Hyodo et al.,

1991; Vaid et al., 2001; Yang and Sze, 2011; Chiaro et al., 2012; Wichtmann and Triantafyllidis, 2016; Pan and Yang, 2018). Take the conventional cyclic triaxial test as an example. The initial static shear stress q_s is often presented in the normalized form of static stress ratio $SSR = q_s/2p_0$, where p_0 is the initial mean effective stress. The subsequent cyclic shear stress q_{cyc} is also often normalized by p_0 and presented as the cyclic stress ratio $CSR = q_{cyc}/2p_0$. For medium dense and dense sands, cyclic mobility deformation mode happens when $q_s < q_{cyc}$ or $SSR < CSR$ as illustrated in Figure 1(a), where transient states of nearly zero mean effective stress p is expected along with the undrained cyclic shearing. This is because an excursion with vanishing deviatoric stress q is a prerequisite for nearly zero p (Vaid and Chern, 1983; Kammerer et al., 2005; Yang et al., 2022b). This vanishing of deviatoric stress q during a cyclic loading event is referred to as "stress reversal" or SR. In the absence of stress reversal referred to as "no stress reversal" or NSR, as shown in Figure 1(b), i.e., when $q_s > q_{cyc}$ or $SSR > CSR$, the mean effective stress p stays well above zero, and the internal structure of the granular assembly is expected to

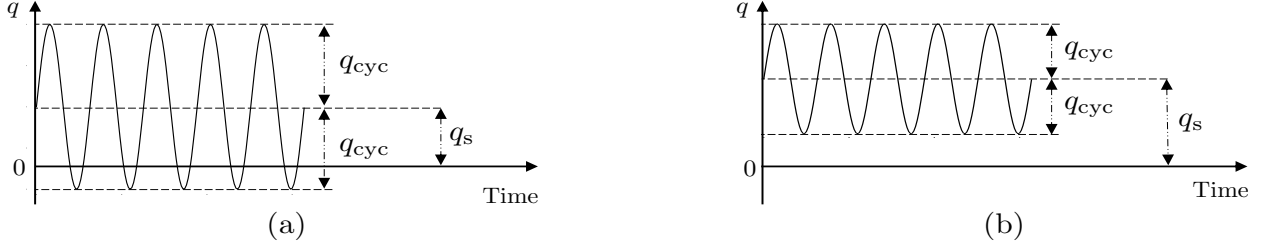


Figure 1. Time histories of shear stress q in undrained cyclic triaxial loading, illustrating the cases (a) experiencing stress reversal (SR), and (b) not experiencing stress reversal (NSR).

maintain its connectivity, and consequently the granular system is not expected to experience a collapse due to cyclic loading. The repeated loading exerted on the rather stable sample, however, will cause progressive accumulation of shear strain in each loading cycle, or cyclic ratcheting (Alonso-Marroquin and Herrmann, 2004).

Despite all these different deformation modes in undrained cyclic shearing, a criterion should be adopted to signify the initiation of an undesirable response in various scenarios of cyclic loading of sands. While the null mean effective stress criterion, or perhaps more accurately when p drops to a residual value close to zero (Yang et al. 2021), which signifies the initial liquefaction (IL), works well for flow liquefaction, or for cyclic mobility in SR cases, one would expect that this criterion becomes invalid for the case of NSR that lead to residual deformation accumulation, given that p does not get a chance to reach zero. Instead, a shear strain-based criterion is often adopted. Such criterion is more widely used likely because a considerable amount of shear strain is observed when p vanishes in the scenarios of flow liquefaction or cyclic mobility, and such criterion remains feasible in scenario of residual deformation accumulation for both SR and NSR. Based on Ishihara (1993) reaching 5% double-amplitude (DA) axial strain is chosen to characterize the cyclic loading resistance for the mode of cyclic mobility. In the mode of residual deformation accumulation, however, as the strain develops only in one direction, a single amplitude (SA) axial strain criterion is more reasonable to be adopted (Yang and Sze, 2011). While some studies (e.g., Hyodo et al., 2002; Yang and Sze, 2011) used 5% SA axial strain as a failure criterion, here we adopt a 2.5% SA axial strain to quantify the cyclic resistance.

Numerous studies have been built on strain-based failure criteria, such as investigating the impact of initial static shear stress on the cyclic resistance (e.g., Vaid et al., 2001), introducing the so-called K_α effect (Seed, 1983), and validating the sand constitutive models via this criterion. Still, one may wonder about the fundamental reason behind these cyclic deformations that lead to adopting such straightforward strain-based criteria, especially for the case of cyclic shearing with residual deformation accumulation.

To provide insights into this question, we resort to the “numerical experiments” obtained from the discrete element method (DEM). By directly modeling the kinematics of each particle in the granular assembly, DEM can be used as a suitable platform that investigates the mechanical response of the granular materials, from both

macroscopic (homogenized) and grain-scale perspectives. In the past decades, DEM has been widely used to study the cyclic liquefaction of granular materials (e.g., Sitharam, 2003; Kuhn et al., 2014; Barrero et al., 2018; Huang et al., 2018; Yang et al., 2021). More recently, Wu et al. (2021) explored the coaxiality between the strain increment (loading) direction and the contact-normal based fabric behind the cyclic mobility and the residual deformation accumulation. Yang et al. (2022b) studied the evolution of microstructure under multidirectional cyclic loadings with different paths, revealing the internal structure stability for the cases without experiencing transients of zero p where $SSR > CSR$. This paper adopts a three-dimensional (3D) DEM to perform constant-volume cyclic triaxial simulations to shed some light on the two different deformation modes in dense granular materials, i.e., cyclic mobility and the residual deformation accumulation. We first present the details of sample preparation and simulation protocols. Then we analyze the simulation results from both macroscopic and microscopic levels, where laboratory experiments are also used to support the observed outcome and the resulting claim from those.

2 NUMERICAL PROCEDURE

The open-source DEM software LIGGGHTS (Kloss et al., 2012) is used in this study to carry out the constant-volume cyclic triaxial simulations of a granular assembly. The particles interact based on a soft-particle law, allowing slight overlap at the contact points. The contact laws consist of a Hertzian normal model and a history-dependent tangential model with a Coulomb cut-off. The modified elastic-plastic spring dashpot (EPSD) (Ai et al., 2011) is adopted to capture the rolling resistance between

Table 1. DEM parameters.

Description	Value
Particle Density, ρ (kg/m ³)	2,650
Young's Modulus, E (GPa)	70
Poisson's ratio, μ	0.3
Coefficient of restitution, ϵ	0.8
Tangential friction, μ_t	0.5
Rolling friction, μ_r	0.35
Rolling viscous damping, η_r	0.13

particles. The DEM input parameters adopted for the simulations are listed in Table 1.

The simulations in this paper involve two stages: (1) preparing a particle assembly with the target consolidation state and (2) applying cyclic triaxial shearing to the assembly under constant-volume conditions. The gravity is set to zero during the simulation to avoid any stress gradient. The particle assembly in this study includes 15,625 spheres with the grain size distribution following that of Ottawa F65 sand. The particle diameters are in the range 0.12–0.36 mm. Generated particles are randomly placed on a 3D sparse lattice to avoid overlap, like the approach followed by Mutabaruka et al. (2019). This 3D lattice is then encompassed by three pairs of periodic boundaries, to eliminate the local inhomogeneities in this representative volume element of a triaxial test (Lopera Perez et al., 2015). The sample preparation stage consists of four sub-stages. i) The sparse particle assembly is isotopically compressed via translationally moving six periodic boundaries inward to reduce the void ratio to $e = 1.2$. In this sub-stage, particles start to come in contact with each other. ii) A servo-control isotropic compression algorithm to compress the sample until reaching 10% of desired confining stress, implying the formation of stable contact network in the particle assembly. iii) Continuing the isotropic compression until the mean stress reaches the desired value (100 kPa in this study). iv) A desired deviatoric stress is imposed on the sample while preserving the mean stress, i.e., following a constant- p stress path. During the sample compression, the tangential friction coefficient μ_t is tuned in sub-stages i and ii to construct samples with varying densities. The μ_t is then set to 0.5 in the last two sub-stages, and also in the subsequent stage of cyclic shearing. One can refer to Yang (2020) for the details. This paper adopts $\mu_t = 0.2$ in the first two sub-stages of sample preparation to obtain a dense sample with $e = 0.637$. Figure 2 shows the particle arrangement at the end of sample preparation.

In the cyclic triaxial shearing stage, constant volume is maintained by restraining the volumetric strain rate of the sample to zero, i.e., $\dot{\epsilon}_v = \dot{\epsilon}_a + 2\dot{\epsilon}_r = 0$, with the $\dot{\epsilon}_a$ and $\dot{\epsilon}_r$ being the rates of axial and radial strains, respectively. The shearing is imposed at a constant velocity along the axial direction via v_a . Once the absolute value of the deviatoric stress q reaches the upper or lower limits of cyclic

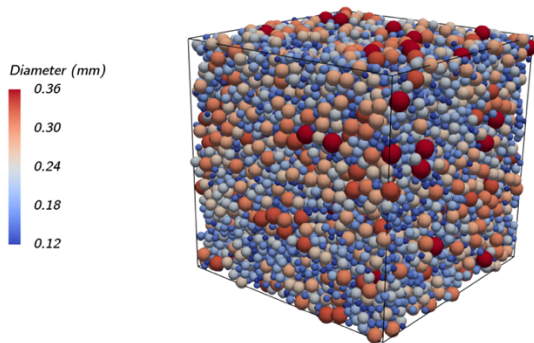


Figure 2. Illustration of particle arrangements at the end of the sample preparation.

deviatoric stress, $q_{\max} = q_s + q_{\text{cyc}}$ or $q_{\min} = q_s - q_{\text{cyc}}$, respectively, the axial loading direction is reversed.

The axial velocity v_a chosen in the shearing stage is small enough to ensure that the system maintains the quasi-static regime before p gets close to zero, i.e., the inertial number $I = \dot{\gamma}d\sqrt{\rho/p} < 10^{-3}$ (GDR MiDi 2004). Here $\dot{\gamma} = v_a/h$, d is the minimum diameter of particles, ρ is the particle density, p is the mean effective stress, and h is the sample height. At very low p when the sample liquefies, I transiently becomes larger than the threshold. Further decreasing v_a to keep I below the threshold will increase the simulation time tremendously but has been observed to not affect the simulation results noticeably. Thus, the value of v_a is chosen so that $I < 10^{-3}$ when $p \geq 1$ kPa.

3 MACROSCOPIC RESPONSE

The stress tensor σ within the granular assembly is calculated based on the Love-Weber formula:

$$\sigma = \frac{1}{V} \sum_{c \in N_c} \mathbf{l}^c \otimes \mathbf{f}^c, \quad [1]$$

where \mathbf{l}^c is the branch vector connecting the centers of two particles, \mathbf{f}^c is the contact force, \otimes denotes the dyadic tensor product, and the summation runs over all the contacts N_c in the selected volume V . The mean effective stress p and deviatoric stress q can be determined from the stress tensor, i.e., $p = (\sigma_{xx} + \sigma_{yy} + \sigma_{zz})/3$ and $q = \sigma_{zz} - \sigma_{xx}$, where axis z is considered along the axial loading direction of the particle assembly.

The change in distance between a pair of periodic boundaries normal to a particular direction over the initial distance at the beginning of the shearing stage represents the strain in a particular direction. Single amplitude (SA) axial strain is defined as the maximum absolute value of axial strain in a loading cycle. The difference between the maximum and minimum axial strains in a loading cycle represents the double amplitude (DA) of axial strain.

To study the effect of initial static shear on the undrained cyclic response, anisotropically compressed samples are prepared and then are subjected to constant-volume cyclic triaxial shearing under different CSR values. Table 2 lists the performed simulations. Additional simulations were also carried out for CSR = 0.05 but they did not reach the failure criterion in the first 400 loading cycles and therefore their results are not presented in this paper. Two of the simulations from Table 2 are selected here to illustrate the effect of SSR on the macroscopic

Table 2. Loading conditions of performed simulations, underlining the selected cases for detailed assessment in Figs. 3-5 and 8-9.

Test	SSR	CSR
1-4	0.10	0.10, 0.15, 0.20, 0.25
5-8	<u>0.15</u>	<u>0.10</u> , 0.15, <u>0.20</u> , 0.25
9-13	0.20	0.10, 0.15, 0.20, 0.25, 0.30

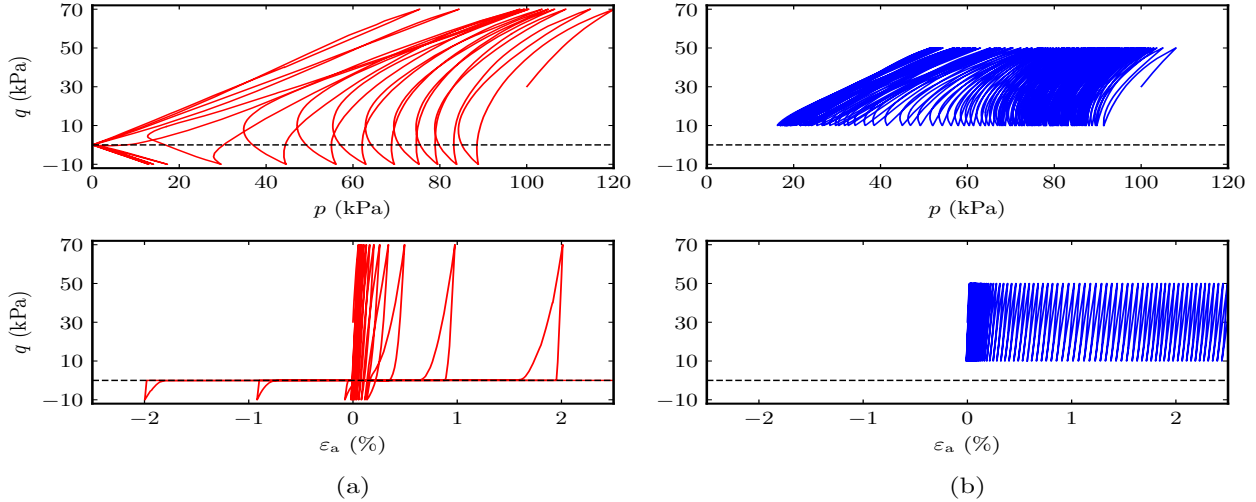


Figure 3. Typical simulation results of stress-strain response for two loading scenarios: (a) $SSR=0.15$ and $CSR=0.20$ hence experiencing SR and cyclic mobility, and (b) $SSR=0.15$ and $CSR=0.10$ hence experiencing NSR and residual deformation accumulation.

response: $CSR = 0.10$ and 0.20 on the sample with $SSR = 0.15$, as displayed in Figure 3. In both cases, as cyclic shearing continues, the stress path oscillates up and down, and moves toward to the left (decreasing mean effective stress). The case of $CSR = 0.20$ in Figure 3(a) involves SR, hence it goes through reduction of p to nearly zero, referred to as liquefaction. Then the stress path evolves along a stabilized non-symmetrical butterfly shape, in which it transiently undergoes the state of nearly zero p twice during each loading cycle, where large shear strain accumulations occur. One can simply use a p threshold (e.g., 5 kPa) to represent the transition between solid-like to fluid-like states. The special treatment of stress-strain response when mean stress drop below such threshold level has also been used recently in the form of a defining a “semifluidized state” for the purpose of constitutive modeling of sands in post-liquefaction cyclic shearing (Barrero et al. 2020, and Yang et al. 2022a). The fluid-like states correspond to a regime with low shear modulus, decreasing dilatancy, and reduced shear viscosity as shown in Yang et al. (2022c).

Such threshold p , however, is not reached in the case of $CSR = 0.10$ in Figure 3(b), which involves NSR, and subsequently p stays above 15 kPa after many loading cycles. Such large p implies the existence of well-connected force chains in the granular assembly which can sustain the external medium shear without reaching the yielding flow as usually seen at critical state. As a result, the corresponding shear strain accumulates cycle by cycle, due to the different stiffnesses in the loading and unloading periods (Alonso-Marroquin and Herrmann 2004). Although the loading scenario of Figure 3(b) does not exhibit instantaneous large variations of axial strain as observed in the loading scenario of Figure 3(a), it still develops considerably large axial strains in larger number of loading cycles. In view of this, often the same strain threshold used for identifying the cyclic liquefaction resistance is applied to analyzing the results of both loading scenarios. While such strain threshold is likely associated with the initiation of

fluid-like state in the former case, it is associated with a very different mechanism of response for the latter case.

Figure 4 presents the axial strain development for both cases of SR and NSR. In the SR case, axial strain starts to accumulate in a non-symmetrical pattern until reaching the IL where the normalized mean stress drops below 0.05 for the first time. Beyond the IL, the strain develops considerably in each half cycle, and the overall accumulation for the loading scenario presented here is toward the compression side, i.e. the same direction of the static shear stress. The axial strain development pattern of the NSR case is completely different. While in each cycle the amplitude of strain is relatively small, shearing in many cycles result in development of axial strain along the compression side, the so-called residual deformation accumulation.

To further compare both SR and NSR loading conditions and assess the relevance of the conventional cyclic resistance criteria, we plot the evolutions of normalized mean stress and single amplitude (SA) axial

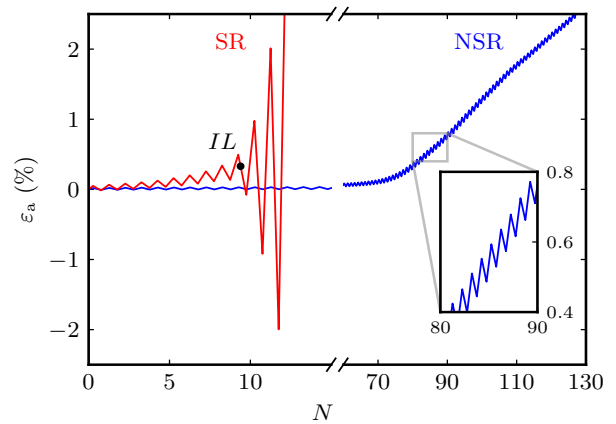


Figure 4. Development of axial strains in simulation of the tests in Figure 3, involving SR and NSR.

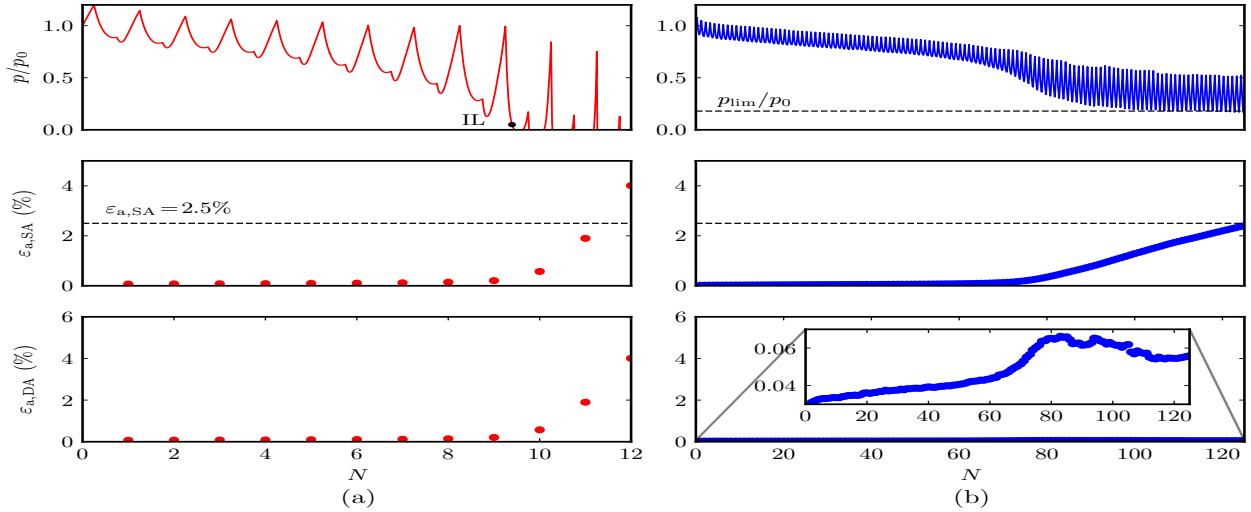


Figure 5. Variations of normalized mean stress, SA axial strain, and DA axial strain during the subsequent loading cycles for the two tests presented in Figure 3: (a) a case with SR and (b) a case with NSR.

strain as well as double amplitude (DA) axial strain in Figure 5. In the cyclic mobility case, shown in Figure 5(a), the mean stress drops to near zero, hence a stress-based criterion, i.e., mean stress drops below a threshold, can be used to signify the IL. We see both SA and DA axial strains have relatively small values before reaching IL. After IL, as a result of transition to fluid-like state, both start to increase, therefore, a criterion based on SA or DA axial strain becomes relevant to characterize the cyclic resistance. In the residual deformation mode, however, mean stress technically cannot reach low values, as shown in Figure 5(b). This shows that stress-based criterion is not always practical to signify the failure when the sample is under initial static shear. Depending on the loading conditions, the normalized mean stress cannot drop below a limiting minimum value denoted as p_{lim}/p_0 , as illustrated also in

Figure 5(b). As the axial strain develops in the form of cyclic ratcheting (Alonso-Marroquin and Herrmann, 2004), several researchers have been using a SA axial strain threshold to signify the cyclic resistance (e.g. Hyodo et al., 2002; Yang and Sze, 2011). DA axial strain in the residual deformation mode initially increases at a small rate, shows a relative peak value in this simulation, and subsequently reaches a plateau. Near the state of DA strain reached a plateau, the normalized mean effective stress also reaches a stabilized pattern with nearly constant oscillation magnitudes. As a result of cyclic ratcheting, DA axial strain has small values in cases of residual deformation accumulation and it is far below the threshold adopted by former researchers (e.g., Ishihara, 1993), hence it cannot be used as a failure criterion.

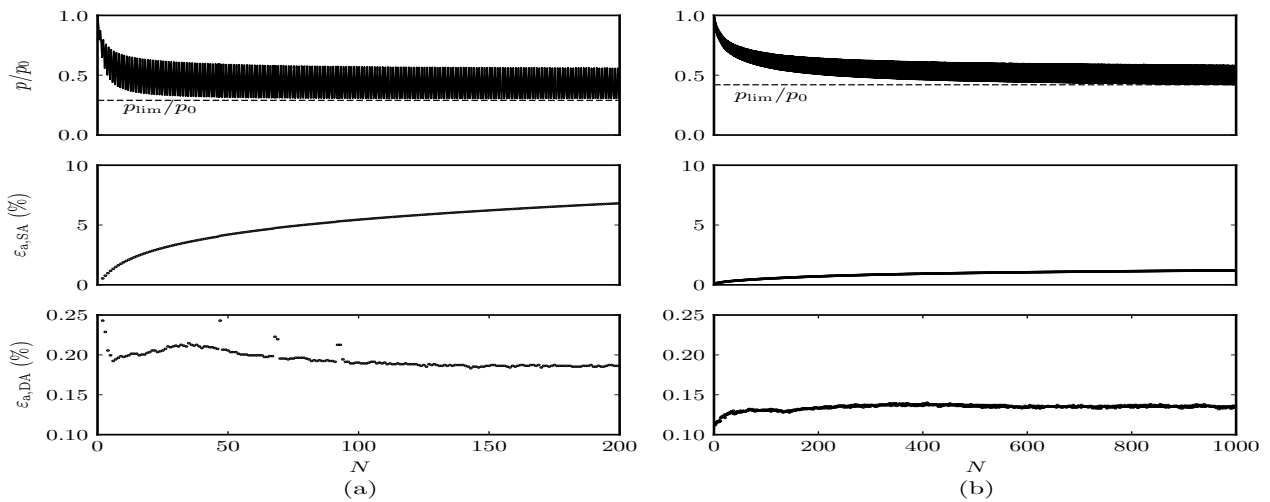


Figure 6. Variations of normalized mean stress, SA axial strain, and DA axial strain for laboratory experiments on Karlsruhe fine sand, under $p_0 = 300$ kPa, $SSR = 0.25$, and $CSR = 0.20$ on two samples with relative densities of (a) 61% and (b) 86%. Data from Wichtmann and Triantafyllidis (2016) TCUA6 and TCUA8 tests.

To check the occurrence of p_{lim} and the saturation state of DA axial strain in the laboratory experiments for cases of NSR, we also present the undrained cyclic triaxial experimental data from Wichtmann and Triantafyllidis (2016) for two selected tests on Karlsruhe fine sand at relative densities of 61% and 86%. Based on these physical test data, we generate similar plots to Figure 5 as shown in Figure 6. Clearly, both cases present the occurrence of p_{lim} and the saturation of DA axial strain.

Figure 7(a) shows the limiting normalized mean stress p_{lim}/p_0 for different simulations. In the SR and SSR = CSR modes, mean stress drops to near zero values and technically these samples can reach liquefaction. In NSR mode, on the other hand, different limits are observed based on loading conditions. Considering an SSR value, shearing with lower CSR will increase the p_{lim}/p_0 ratio. Figure 7(b) presents the number of cycles to reach failure based on the 2.5% axial strain threshold. For each color coded SSR value an apparent log-linear pattern of relation can be observed between the SSR/CSR and N_f , which moves rightward with the increase of SSR. Further simulations may be needed to further confirm this observation. Figure 7(c) shows cyclic resistance curves for different SSR values. For the dense sample used in this

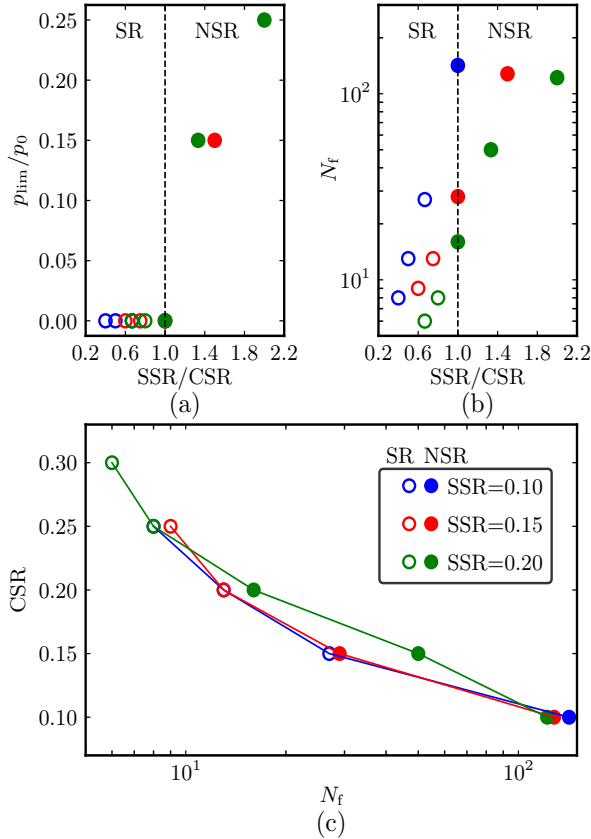


Figure 7. (a) Limit values of normalized mean stress, p_{lim}/p_0 , (b) number of cycles to reach failure based on 2.5% axial strain, N_f , for different levels of SSR/CSR, and (c) cyclic resistance curves for different SSR values based on 2.5% axial strain failure criterion.

study, the cyclic resistance curves appear to be fairly close to each other. Further simulations on different sample densities would illustrate better the effect of SSR on the cyclic resistance.

4 MICROSTRUCTURE

In this section we adopt coordination number and particle connectivity to reveal the internal structure evolution of the granular assembly in the constant-volume cyclic triaxial simulations.

Coordination number, defined as the average number of contacts per particle, is a scalar quantity describing the contact network and can approximate the level of static redundancy, i.e., the difference between the average number of constraints for a particle and its degrees of freedom (Radjai et al., 2004; Yang et al., 2021). Here the geometrical coordination number z_g is used, neglecting the particles with no contacts, i.e., floaters.

Figure 8 shows the evolution of coordination number for the two tests presented in Figure 3. In the case of SR, after reaching the initial liquefaction, coordination number oscillates with high amplitudes, transiently reaching as low as 1.0 which indicates the collapse of contact network. In the case of NSR, the coordination number gradually decreases but always stays above 3.0, implying the stability of the granular system (Yang et al., 2022b). The increasing amplitude of oscillations may suggest a change in internal structure which stabilizes after a transition zone. The inset plots show either the cycle where the IL happens for the case with SR, or the cycles in the neighborhood of the relative peak DA axial strain for the case with NSR. One can see a large drop in z_g slightly after IL in the case with SR but this is not observed for the other case.

To better understand the evolution of the contact network during a loading cycle, we use the connectivity of particles p_c , defined as the proportion of particles with exactly c contacts. Each plot in Figure 9 shows the

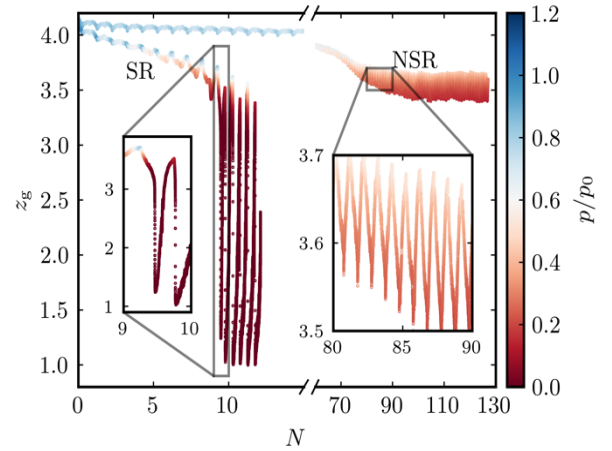


Figure 8. Variation of the coordination number for the two tests presented in Figure 3 with SR and NSR. Inset plots show the IL state for the case with SR and the cycles close to relative peak DA axial strain for the case with NSR.

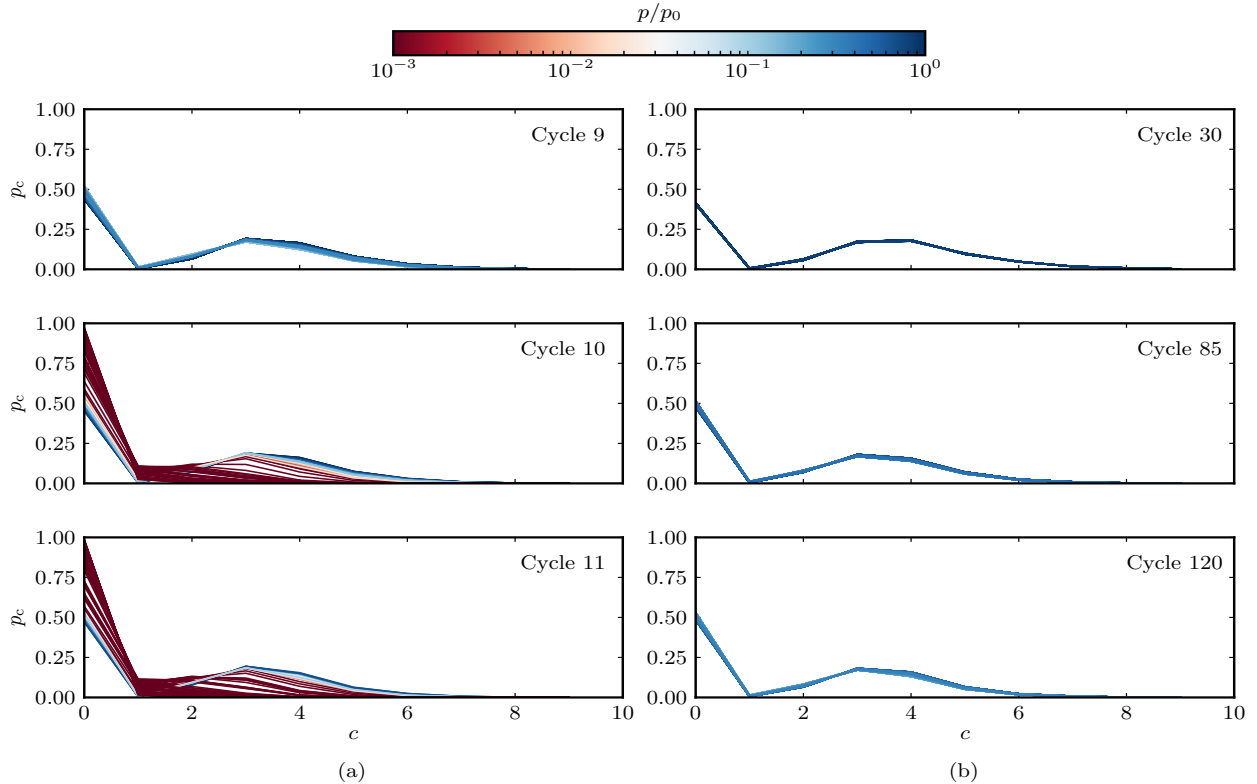


Figure 9. Connectivity of particles during selected loading cycles for the two tests presented in Figure 3: (a) a case with SR and (b) a case with NSR .

connectivity of particles in a loading cycle. For the case of SR, the particle connectivity diagrams do not change noticeably before transitioning to the fluid-like states (cycle 9). However, in cycle 10 with fluid-like states for the first time, there are moments in which the fraction of floaters, particles with no contact, increases dramatically corresponding to the low values of p/p_0 . This pattern is repeated in the subsequent cycle 11. For the case of NSR, the particle connectivity diagram does not change in a noticeable way during the whole shearing process, indicating the stability of the contact network. This is linked to the small variations of DA axial strain during the shearing process. The progressive axial strain accumulation is mainly induced by the incremental slippage during subsequent loading-unloading cycles.

5 SUMMARY

This paper adopts 3D-DEM to investigate the response of dense granular materials under constant-volume cyclic triaxial shearing. The combined effects of initial static shear stress magnitude and cyclic shear stress amplitude on the mechanical behavior of the virtual sample including cyclic mobility and residual deformation accumulation modes are illustrated in the performed numerical experiments. Failure in the cyclic mobility mode, which can happen in loading scenarios with SR, can be signified by either a stress-based criterion, i.e., mean stress drops below a threshold,

or a strain-based criterion, e.g., a threshold on SA or DA axial strain. However, only SA axial strain is a feasible failure criterion for the residual deformation mode. For this latter mode, which can happen in loading scenarios with NSR, we observe that with increasing the number of loading cycles the DA axial strain shows an apparent peak and reaches a plateau. Plotting the number of cycles to failure based on SSR/CSR ratios was showing a linear trend for certain SSR values. Cyclic resistance curves for different initial static shear stresses are close to each other for the relatively dense sample studied here. Further simulations on looser samples would allow for more comprehensive study of the effect SSR on cyclic resistance. In addition, we investigate the evolution of contact-based microstructure for the simulations showing cyclic mobility and residual deformation accumulation. The former presents the collapse of the contact network in the fluid-like states while the latter always stays stable. In cyclic mobility mode, both coordination number and connectivity of particles show dramatic changes in each loading cycle. On the other hand, in the residual deformation accumulation, the internal structure is relatively stable.

ACKNOWLEDGEMENT

Financial support for this study was provided by the Natural Sciences and Engineering Research Council of Canada (NSERC).

REFERENCES

- Ai, J., Chen, J.F., Rotter, J.M. and Ooi, J.Y., 2011. Assessment of rolling resistance models in discrete element simulations. *Powder Technology*, 206(3), 269-282.
- Alonso-Marroquin, F. and Herrmann, H.J., 2004. Ratcheting of granular materials. *Physical Review Letters*, 92(5), 054301.
- Barrero, A.R., Oquendo, W., Taiebat, M., Lizcano, A., 2018. Cyclic shearing response of granular material in the semi-fluidized regime. In *Geotechnical Earthquake Engineering and Soil Dynamics V: Numerical Modeling and Soil Structure Interaction*. 100-107.
- Barrero, A.R., Taiebat, M., Dafalias, Y.F., 2020. Modeling cyclic shearing of sands in the semifluidized state. *Int. J. Numer. Anal. Methods Geomech.* 44 (3), 371-388.
- Chiaro, G., Koseki, J. and Sato, T., 2012. Effects of initial static shear on liquefaction and large deformation properties of loose saturated Toyoura sand in undrained cyclic torsional shear tests. *Soils and Foundations*, 52(3), 498-510.
- GDR MiDi. 2004. On dense granular flows, *The European Physical Journal E*, 14, 341-365.
- Huang, X., Kwok, C.Y., Hanley, K.J. and Zhang, Z., 2018. DEM analysis of the onset of flow deformation of sands: linking monotonic and cyclic undrained behaviours. *Acta Geotechnica*, 13(5), 1061-1074.
- Hyodo, M., Hyde, A.F., Aramaki, N. and Nakata, Y., 2002. Undrained monotonic and cyclic shear behaviour of sand under low and high confining stresses. *Soils and Foundations*, 42(3), 63-76.
- Hyodo, M., Murata, H., Yasufuku, N. and Fujii, T., 1991. Undrained cyclic shear strength and residual shear strain of saturated sand by cyclic triaxial tests. *Soils and Foundations*, 31(3), 60-76.
- Ishihara, K., 1993. Liquefaction and flow failure during earthquakes. *Geotechnique*, 43(3), 351-451.
- Kammerer, A.M., Pestana, J.M. and Seed, R.B., 2005. Behavior of Monterey 0/30 sand under multidirectional loading conditions. In *Geomechanics: testing, modeling, and simulation*, 154-173.
- Kloss, C., Goniva, C., Hager, A., Amberger, S. and Pirker, S., 2012. Models, algorithms and validation for opensource DEM and CFD-DEM. *Progress in Computational Fluid Dynamics, An International Journal*, 12(2-3), 140-152.
- Kuhn, M.R., Renken, H.E., Mixsell, A.D. and Kramer, S.L., 2014. Investigation of cyclic liquefaction with discrete element simulations. *Journal of Geotechnical and Geoenvironmental Engineering*, 140(12), 04014075.
- Lopera Perez, J.C., Kwok, C.Y., O'Sullivan, C., Huang, X. and Hanley, K.J., 2015. Numerical study of one-dimensional compression in granular materials. *Géotechnique Letters*, 5(3), 96-103.
- Mutabaruka, P., Taiebat, M., Pellenq, R.J.M. and Radjai, F., 2019. Effects of size polydispersity on random close-packed configurations of spherical particles. *Physical review E*, 100(4), 042906.
- Pan, K. and Yang, Z.X., 2018. Effects of initial static shear on cyclic resistance and pore pressure generation of saturated sand. *Acta Geotechnica*, 13(2), 473-487.
- Radjai, F., Trodec, H. and Roux, S., 2004. Key features of granular plasticity. *Granular materials: Fundamentals and applications*, 157-184.
- Seed, H. B., 1983. Earthquake resistant design of earth dams, in *Proceedings, Symposium on Seismic Design of Embankments and Caverns*, Pennsylvania, ASCE, NY, pp. 41-64.
- Sitharam, T., 2003. Discrete element modelling of cyclic behaviour of granular materials. *Geotechnical & Geological Engineering*, 21(4), 297-329.
- Vaid, Y.P. and Chern, J.C., 1983. Effect of static shear on resistance to liquefaction. *Soils and foundations*, 23(1), 47-60.
- Vaid, Y.P., Stedman, J.D. and Sivathayalan, S., 2001. Confining stress and static shear effects in cyclic liquefaction. *Canadian Geotechnical Journal*, 38(3), 580-591.
- Wichtmann, T. and Triantafyllidis, T., 2016. An experimental database for the development, calibration and verification of constitutive models for sand with focus to cyclic loading: part I - tests with monotonic loading and stress cycles. *Acta Geotechnica*, 11(4), 739-761.
- Wu, Q.X., Pan, K. and Yang, Z.X., 2021. Undrained cyclic behavior of granular materials considering initial static shear effect: Insights from discrete element modeling. *Soil Dynamics and Earthquake Engineering*, 143, 106597.
- Yang, J. and Sze, H.Y., 2011. Cyclic behaviour and resistance of saturated sand under non-symmetrical loading conditions. *Géotechnique*, 61(1), 59-73.
- Yang, M., 2020. *Micro- and micromechanical modeling of granular material under constant volume cyclic shearing* (Ph.D. thesis). University of British Columbia, Vancouver, Canada.
- Yang, M., Taiebat, M., Mutabaruka, P. and Radjai, F., 2021. Evolution of granular materials under isochoric cyclic simple shearing. *Physical Review E*, 103(3), 032904.
- Yang, M., Taiebat, M., Dafalias, Y.F., 2022a. SANISAND-MSf: a sand plasticity model with memory surface and semifluidised state. *Géotechnique* 72 (3), 227-246.
- Yang, M., Taiebat, M., Mutabaruka, P. and Radjai, F., 2022b. Evolution of granular media under constant-volume multidirectional cyclic shearing. *Acta Geotechnica*, 17(3), 779-802.
- Yang, M., Taiebat, M. and Radjai, F., 2022c. Liquefaction of granular materials in constant-volume cyclic shearing: Transition between solid-like and fluid-like states. *Computers and Geotechnics*, 148, 104800.